

See discussions, stats, and author profiles for this publication at: <https://www.researchgate.net/publication/5926130>

Molecular Simulations of Droplet Coalescence in Oil/Water/Surfactant Systems

ARTICLE *in* THE JOURNAL OF CHEMICAL PHYSICS · NOVEMBER 2007

Impact Factor: 2.95 · DOI: 10.1063/1.2780865 · Source: PubMed

CITATIONS

36

READS

108

2 AUTHORS, INCLUDING:



Daan Frenkel

University of Cambridge

549 PUBLICATIONS 27,084 CITATIONS

SEE PROFILE

Molecular simulations of droplet coalescence in oil/water/surfactant systems

Live Rekvig^{a)} and Daan Frenkel

FOM Institute for Atomic and Molecular Physics, Kruislaan 407, 1098 SJ Amsterdam, The Netherlands

(Received 17 July 2007; accepted 16 August 2007; published online 2 October 2007)

We report a molecular simulation study of the mechanism by which droplets covered with a surfactant monolayer coalesce. We study a model system where the rate-limiting step in coalescence is the rupture of the surfactant film. Our simulations allow us to focus on the stages at the core of the coalescence process: the initial rupture of the two surfactant monolayers, the rearrangement of the surfactant molecules to form a channel connecting the two droplets, and the expansion of the radius of the resulting channel. For our numerical study, we made use of the dissipative particle dynamics method. We used a coarse-grained description of the oil, water, and surfactant molecules. The rupture of the surfactant film is a rare event on the molecular time scale. To enhance the sampling of the rupture of the surfactant film, we used forward flux sampling (FFS). FFS not only allows us to estimate coalescence rates, it also provides insight into the molecular structure and free energy of the “transition” state. For an oil-water-oil film without surfactant, the rupture rate decreases exponentially with increasing film thickness. The critical state is different in thin and thick films: Thin films break following a large enough thickness fluctuation. Thicker films break only after a sufficiently large hole fluctuation—they can heal. Next, we designed surfactant molecules with positive, zero, and negative natural curvatures. For a water film between two surfactant-covered oil droplets, the rupture rate is highest when the surfactant has a negative natural curvature, lowest when it has zero natural curvature, and lying in between when it has a positive natural curvature. This nonmonotonic variation with curvature stems from two effects: First, the surfactants with a large absolute value of the natural curvature have lower interfacial tension and bending rigidity. This promotes the interfacial fluctuations required to nucleate a channel. Second, the sign of the natural curvature determines whether there is a critical channel radius at which the channel free energy has a maximum. The latter is in agreement with the hole-nucleation theory of Kabalnov and Wennerström [Langmuir **12**, 276 (1996)]. Our simulations seriously overestimate the relative stability of surfactant free emulsions. We argue that this is due to the fact that our model does not allow for nanobubble formation and capillary evaporation—processes that are presumably of key importance in the coalescence of surfactant-free emulsions. © 2007 American Institute of Physics. [DOI: [10.1063/1.2780865](https://doi.org/10.1063/1.2780865)]

I. INTRODUCTION

Droplet coalescence is a ubiquitous phenomenon that plays an important role in many industrial processes, ranging from crude oil recovery to the manufacture of cosmetics and pharmaceutical products or the processing of food products.¹ In the oil industry, a key challenge is to separate oil droplets from the water phase; here coalescence is desirable. In contrast, in the processing of food and pharmaceutical products, droplet coalescence is undesirable because it may lead to macroscopic phase separation.

It has long been realized that, even though water-in-oil and oil-in-water emulsions are thermodynamically unstable, surfactants can make them kinetically stable by inhibiting the coalescence process. Surfactants affect the coalescence rate in several ways:² the surfactant molecules self-assemble into a monolayer at the oil/water interface, thereby changing the probability of film rupture. The surfactant monolayer also

modifies the droplet-droplet interaction. Finally, surfactant aggregates can alter the hydrodynamic properties of the continuous phase, and with them the droplet collision rate.

Emulsion stability is a complex problem due to the large range of time and length scales involved: The droplets typically have sizes in the range of 1 μm –1 mm, but coalescence begins on the nanometer scale, when surfactant molecules on the surfaces of two adjacent droplets come into interaction with each other. Emulsions may phase separate (“break”) within seconds, or remain stable for months, yet the molecular reorientations at the contact point typically take a few nanoseconds. Thus, it is clearly necessary to use a modeling approach that bridges these diverse time scales.

The coalescence rate equals the droplet collision rate times the probability that two colliding droplets will actually coalesce. In some cases, for example, in the absence of surfactant, the emulsion lifetime is mainly dictated by the collision rate. The rate-limiting step is then the hydrodynamics.

Other emulsions rapidly cream or sediment, resulting in one pure phase and one phase of closely packed (possibly

^{a)}Electronic mail: rekvig@amolf.nl

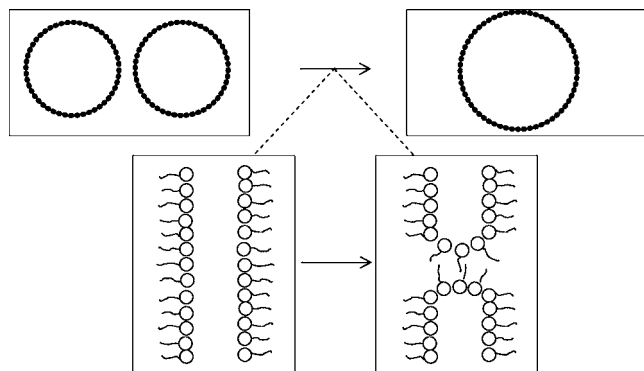


FIG. 1. Schematic drawing of the early stages of droplet coalescence. When two surfactant-covered droplets coalesce, the two monolayers must merge. In order for droplets to merge, the surfactants must reorient and rearrange to form a channel. Expansion of the channel radius completes the coalescence process.

deformed) droplets. The stability of the latter phase depends on the properties of the film separating the droplets, in particular, on the two surfactant monolayers, and the rate at which they rupture and merge. Such metastable creams are the object of this study.

The coalescence rate in dense droplet phases depends strongly on the nature of the surfactants. Furthermore, for a given surfactant, the stability can be tuned by adjusting the temperature (for nonionic surfactants) or the salinity (for ionic surfactants). Experiments do not provide detailed, microscopic information about the mechanism by which two surfactant monolayers merge (a schematic picture is shown in Fig. 1), and it is precisely this aspect that we study by molecular simulation.

Although molecular simulation is an attractive tool to study the early stages of droplet coalescence, fully atomistic simulations are computationally very expensive. As our aim is not to model droplet coalescence for a specific water-oil-surfactant system but rather to correlate the rate and mechanism of coalescence with the physical properties of the surfactant layer, we can use a mesoscopic model that is computationally much cheaper. In the present study, we employed dissipative particle dynamics (DPD) simulations of oil, water, and bead-spring surfactant models. The advantage of the DPD approach is that good DPD models for a number of soft-matter systems have been developed during the past decade. Specifically, DPD models have been constructed for polymer mixtures,^{3–5} surfactant monolayers,^{6,7} lipid bilayers,^{8–10} micelles,¹¹ and vesicles.¹²

Importantly, coarse graining gains us one to two orders of magnitude in accessible length and time scales. However, emulsion films can stay intact for seconds, or even months, whereas the film rupture process takes on the order of nanoseconds. Film rupture therefore classifies as a rare event: the waiting time between events exceeds the duration of the event by many orders of magnitude. As a consequence, the probability of observing film rupture during a (coarse-grained) simulation is practically zero, even though the time scale for the rupture event is short enough to be followed by simulation.

There are several ways to resolve this problem. One is

by “forcing” the droplets to coalesce, i.e., by letting them collide with a sufficiently high velocity to force rapid coalescence.^{13–15} However, the droplet speeds are then unrealistically high compared to the molecular velocities and the resulting mechanism of droplet coalescence may be unrealistic. Another method to force rapid coalescence is to bring the surfactant monolayers very close together, by applying a large compressive force.¹⁶ Depending on the surfactant structure and the monolayer separation, film rupture can then sometimes occur within the simulation time. However, very small separations and/or high forces must be applied in order to observe film rupture during such brute-force simulations.

In the present work, we apply a relatively novel simulation technique called forward flux sampling^{17–19} (FFS) to study the spontaneous film rupture under more realistic conditions. FFS is a method that enhances the sampling of rare events, such as the crossing of a high free-energy barrier that separates two (meta)stable states. In our case, the initial metastable state consists of two droplets separated by an intact emulsion film, and the final stable state is one large droplet. The FFS method does not require prior knowledge of the path between the two states. Small fluctuations in the surfactant monolayers are likely to decay. However, we expect that somewhere along the sequence of events (molecular rearrangements, monolayer rupture, and channel formation), there will be a “point of no return,” a point beyond which the droplets are “committed” to coalescence. Beyond this point, the progress of coalescence becomes deterministic. For the purpose of computing rates, this state may be viewed as the final state in the FFS.

Emulsion droplets are typically $1\ \mu\text{m}$ – $1\ \text{mm}$ in diameter. This means that, on the molecular scale, their surfaces are essentially flat. Moreover, creamed and sedimented layers often contain highly deformed droplets that have large, flat, patches also on a larger scale. Film rupture rates are thus reported per unit time and area.^{20,21} We therefore “zoom in” on the interface between two colloidal droplets (see Fig. 2). The simulation box is rectangular with an oil phase on each side, a water film in the middle, and surfactants at the two interfaces. In this way, computer power is focused on the interfacial region, omitting the large fraction of molecules that make up the bulk interior of the droplets and the reservoir of the continuous phase. The reservoir is modeled implicitly, by imposing equilibrium between the film and a bulk reservoir. We use periodic boundary conditions in the two directions parallel to the interfaces. This leaves out hydrodynamic effects such as film draining and flow of surfactants due to gradients in the surface tension. This assumption is reasonable in the regime where film rupture induced by thermal fluctuations is the rate-determining factor for droplet coalescence.

II. THEORY OF COALESCENCE FREE-ENERGY BARRIERS

A. Natural curvature and surfactant shape

The free-energy density f of a surface depends on its local curvature, characterized by the inverse radii of curvature c_1 and c_2 as follows:²²

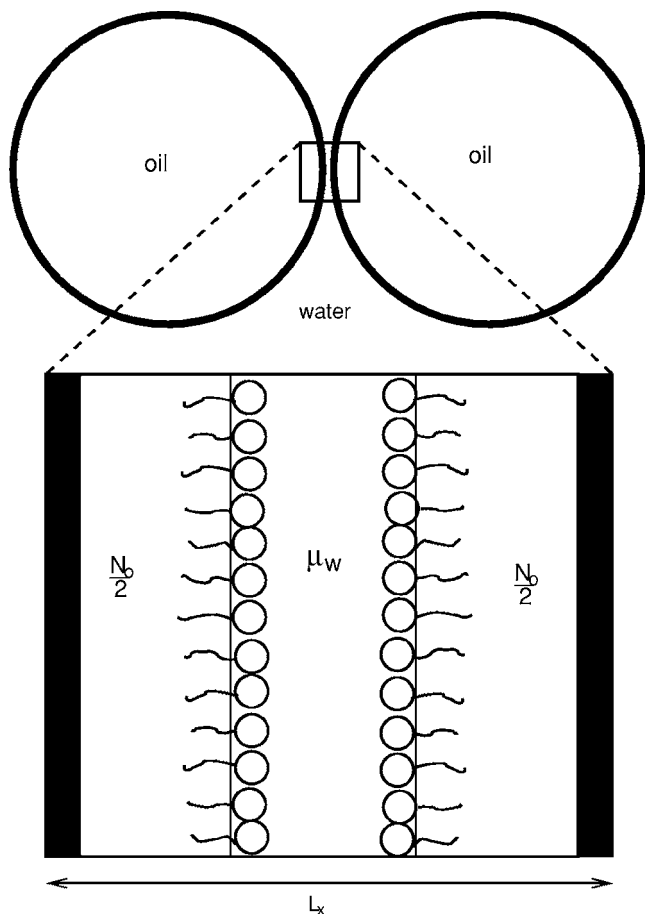


FIG. 2. The simulation system is a “zoom in” on two oil droplets in water. The chemical potential of the water film is fixed so as to mimic the equilibrium with the bulk water reservoir.

$$f(c_1, c_2) \approx \frac{\kappa}{2}(c_1 + c_2 - 2c_0)^2 + \bar{\kappa}c_1c_2. \quad (1)$$

Here c_0 is defined as the curvature that minimizes the free-energy density of the surfactant-coated surface. This natural curvature is sometimes also referred to as the spontaneous curvature. The constant κ describes the bending rigidity of the surface, while the constant $\bar{\kappa}$ describes the free energy cost associated with a local Gaussian curvature c_1c_2 .²² Both the natural curvature c_0 and the constants κ and $\bar{\kappa}$ depend on the shape of the surfactant molecules.

For a given surfactant, a quantitative prediction of c_0 is rarely possible, but one can usually guess its sign and order of magnitude on the basis of the structure and geometric shape of the surfactant. To this end, Israelachvili introduced the concept of a molecular packing parameter V/a_0l_c , where V is the effective hydrocarbon volume, a_0 is the optimum head group surface area, and l_c is the fully extended chain length.²³ The molecular packing parameter depends mainly on the structure of the surfactant, but may vary with temperature or salinity. There is a strong correlation between the molecular packing parameter and the natural curvature of the surfactant. In particular, when $V/a_0l_c \approx 1$, a flat surface is favored ($c_0 \approx 0$), $V/a_0l_c \leq 1$ favors positive curvature $c_0 \geq 0$, and $V/a_0l_c \geq 1$ corresponds to $c_0 \leq 0$.

The equilibrium phase behavior of oil/water/surfactant

systems depends strongly on c_0 : Surfactants with positive curvatures tend to form micelles in water, surfactants with negative curvatures tend to form reverse micelles in oil, and the symmetric ones tend to form lamellae or bicontinuous microemulsions.²³

B. The channel-nucleation theory

Not only the equilibrium phase behavior but also the dynamics of droplet coalescence depend on the natural curvature of the surfactant monolayer.^{24,25} This is not *a priori* obvious as the droplet curvature is several orders of magnitude smaller than the natural curvature associated with the surfactant molecules. However, the natural curvature tends to be of the same order of magnitude as that of the channel that forms between two droplets during the initial stage of coalescence (see Fig. 1). Kabalnov and Wennerström showed that the free energy of the channel depends strongly on c_0 .²⁴ In the channel state, the surfactant monolayers are bent. If the bending is against the natural curvature, channel formation involves a free-energy cost proportional to the bending rigidity κ . If the bending leads to a local curvature that is close to c_0 , the free-energy cost of channel formation tends to be small. Note that the channel is a saddle shape, with two radii of opposite sign. Kabalnov and Wennerström argued that the negative curvature dominates in the case of oil droplets in water. As a consequence, the theory predicts that surfactants with $c_0 > 0$ stabilize oil-water-oil films whereas surfactants with $c_0 < 0$ stabilize water-oil-water films.

In the case of a barrier, the free energy has a maximum at a given channel radius. This radius is the critical radius R^* . 50% of the droplets that reach this stage will go on to coalesce. In the remaining 50%, the channel will shrink again and close, and the two droplets will remain intact. The process is thus akin to other nucleation phenomena, and we will refer to the theory of Ref. 24 as the channel-nucleation theory.

III. MODEL AND SIMULATIONS

A. Dissipative particle dynamics

In DPD,^{3,26,27} conservative (\mathbf{F}^C), random (\mathbf{F}^R), and dissipative (\mathbf{F}^D) forces act between two particles i and j which are a distance r_{ij} apart,

$$\mathbf{F}_{ij} = \mathbf{F}_{ij}^C(r_{ij}) + \mathbf{F}_{ij}^R(r_{ij}) + \mathbf{F}_{ij}^D(r_{ij}). \quad (2)$$

Traditionally, the three forces are

$$\mathbf{F}_{ij}^C = a_{ij}w(r_{ij})\hat{\mathbf{r}}_{ij}, \quad (3)$$

$$\mathbf{F}_{ij}^R = \sigma w(r_{ij})\theta_{ij}\hat{\mathbf{r}}_{ij}, \quad (4)$$

$$\mathbf{F}_{ij}^D = -\eta w^2(r_{ij})(\hat{\mathbf{r}}_{ij} \cdot \mathbf{v}_{ij})\hat{\mathbf{r}}_{ij}. \quad (5)$$

Here, \mathbf{v}_{ij} is the velocity difference between the two particles, $\hat{\mathbf{r}}_{ij}$ is the unit vector pointing from particle i to particle j , θ_{ij} is a randomly fluctuating variable with Gaussian statistics,³ and w is a weight function,

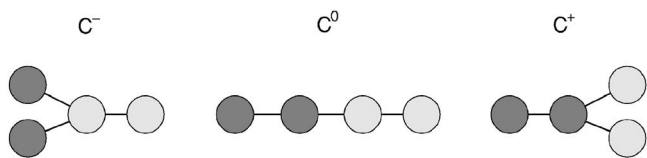


FIG. 3. Schematic illustration of the surfactants used in this study. The light gray particles are hydrophilic/head beads (h) and the dark gray particles hydrophobic/tail beads (t). The surfactants are labeled C^- , C^0 , and C^+ , to reflect that they have negative, zero, and positive natural curvatures, respectively.

$$w(r) = \begin{cases} 1 - r/r_c & \text{for } r < r_c \\ 0 & \text{for } r \geq r_c. \end{cases} \quad (6)$$

a_{ij} , σ , and η determine the amplitude of the conservative, random, and dissipative forces, respectively. The dissipative and random forces act as a thermostat with temperature $\sigma^2/2\eta = k_B T$.²⁷

Integrating the DPD equations self-consistently is non-trivial because the dissipative force depends not only on the particle positions but also on their velocities. To avoid the integration problem we use the thermostat of Peters.²⁸ This thermostat is similar to the Lowe-Anderson thermostat²⁹ in that it is stochastic, local, and Galilean invariant, but it also reduces to the DPD equations of motion in the limit of $\Delta t \rightarrow 0$.

Throughout this paper we use reduced units. The units of length, mass, and energy are the cut-off radius r_c , bead mass m , and k_B times the temperature of the thermostat, respectively.

B. Model

We use a coarse-grained approach where one DPD particle represents a group of atoms, or a liquid volume. Water beads, oil beads, head beads, and tail beads are denoted by w , o , h , and t , respectively. We adopt a minimal model where head beads are identical to water beads, and tail beads are identical to oil beads. Based on Groot³⁰ we use $a_{ww} = a_{oo} = 25$ and $a_{wo} = 80$, where a is defined in Eq. (3).

Water and oil are represented by single beads for simplicity. A surfactant molecule consists of head groups and tail groups connected by harmonic bond and angle potentials. We create three surfactants, shown in Fig. 3, which we label according to their natural curvature c_0 . According to the sign convention, $c_0 > 0$ if the surfactant forms monolayers that prefer to bend towards the oil phase. The surfactants labeled C^- and C^+ have therefore negative and positive natural curvatures, respectively. Due to the symmetry of the model, $c_0 \equiv 0$ for C^0 .

The surfactant bond and angle potentials are

$$U^{\text{bond}} = \frac{k_b}{2} (r_{ij} - r_0)^2, \quad (7)$$

$$U^{\text{angle}} = \frac{k_a}{2} (\theta - \theta_0)^2. \quad (8)$$

We use $k_b = 100$, $k_a = 25$, and $r_0 = 0.7$. For the $h-h-t$ and $h-t-t$ angles, $\theta_0 = 180^\circ$ (each surfactant has two of these) whereas

for the $h-t-h$ angle (for C^+) and $t-h-t$ angle (for C^-), $\theta_0 = 60^\circ$. These model parameters make oil and water immiscible, and the solubility of surfactants in either bulk phase is very low.⁶

The system is a rectangular box of dimensions $L_x \times L_y \times L_z$, with periodic boundary conditions in the y and z directions, and walls at $x=0$ and $x=L_x$. The walls prevent the interfaces from interacting via the oil phase. To limit packing effects, the walls are made softly repulsive as the interparticle potential,

$$\mathbf{F}_i^{\text{wall}} = a_{\text{wall},i} w(|x_{\text{wall},i}|) \hat{\mathbf{x}}_{\text{wall},i}, \quad (9)$$

where $x_{\text{wall},i} = x_{\text{wall}} - x_i$ and $\hat{\mathbf{x}}_{\text{wall},i} = x_{\text{wall},i}/|x_{\text{wall},i}| \hat{\mathbf{x}}$. We chose $a_{\text{wall},i} = a_{\text{oil},i}$. In addition, hard reflective walls prevent particles from crossing the box boundary in the x direction,

$$\text{if } x_i(t + \Delta t) < 0.0 \quad \text{then } x_i(t + \Delta t) := -x_i(t + \Delta t), \quad (10)$$

$$\text{if } x_i(t + \Delta t) > L_x \quad \text{then } x_i(t + \Delta t) := 2L_x - x_i(t + \Delta t). \quad (11)$$

These walls limit the packing effects to two to three units away from the walls.¹⁶

C. Forward flux sampling (FFS)

FFS (Refs. 17–19) is a method to compute the rate, and study the pathway, of rare events. The FFS algorithm generates trajectories in phase space, connecting an initial state, A , and a final state, B . The method works both for equilibrium and nonequilibrium systems. In our system, state A represents two intact monolayers, whereas in state B , the monolayers are connected via a channel, see Fig. 1. Although detailed knowledge of the reaction coordinate is not required for FFS, one must specify a reaction parameter $\lambda(\mathbf{r}_i)$ that is able to distinguish the initial and final states of the rare event. In practice, this means that we have to define $\lambda(\mathbf{r}_i)$ such that $\lambda < \lambda_A$ when the system is in state A and $\lambda > \lambda_B$ if the system is in state B . We choose $\lambda(\mathbf{r}_i)$ as follows: Before film rupture, λ takes the negative value of the minimum thickness of the water layer. After film rupture, λ is the radius of the hole in the water layer. This choice of λ is continuous also in the singularity where the water film breaks and the channel radius is zero. The detailed definition of $\lambda(\mathbf{r}_i)$ is given in Appendix A.

State A is defined by limiting the local water film thickness to λ_A , whereas state B is reached when the channel radius reaches λ_B . Next, one defines a series of n “interfaces” $\lambda_1 \cdots \lambda_n$ such that $\lambda_A < \lambda_1$, $\lambda_i < \lambda_{i+1}$, and $\lambda_n < \lambda_B$. Although the path from A to B is unknown, any path will necessarily pass through every interface. Thus, λ_{i+1} will not be crossed before λ_i , but the coalescence process need not follow a path of monotonically increasing λ (i.e., loops are possible).

If the dynamics of the system has a stochastic component (as is the case for DPD), the problem of computing the (very low) rate k_{AB} can now be decomposed into computing the (larger) flux of trajectories from A to λ_1 , $\Phi_{A,1}$, and the set of probabilities of reaching each interface, given that the previous interface was already reached,

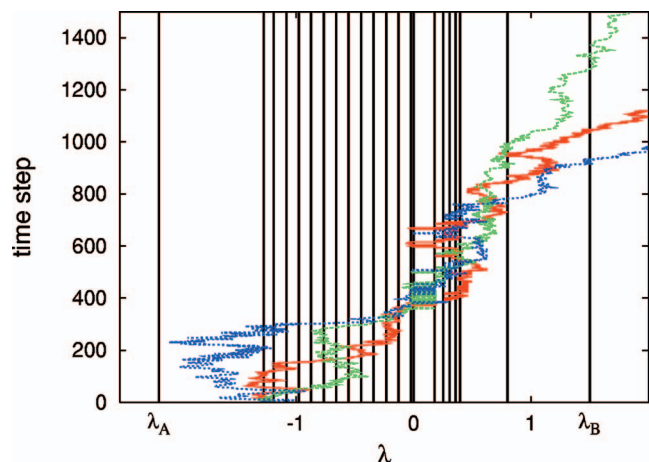


FIG. 4. (Color) Three trajectories connecting states A and B for the system with C^- . The vertical lines are the interfaces employed in the FFS scheme.

$$k_{AB} = \Phi_{A,1} \times P(\lambda_B | \lambda_1), \quad (12)$$

where

$$P(\lambda_B | \lambda_1) = \prod_{i=1}^{n-1} P(\lambda_{i+1} | \lambda_i) \times P(\lambda_B | \lambda_n). \quad (13)$$

The interfaces must be chosen such that $\Phi_{A,1}$ is large enough to be computed in a standard (“brute-force”) simulation: $\Phi_{A,1} = N_1^{\text{succ}} / \tau$, where N_1^{succ} is the number of times a trajectory that starts in A reaches the first interface during a simulation of time τ . During this simulation, the configurations at $\lambda = \lambda_1$ are saved for use as starting configurations for the computation of $P(\lambda_2 | \lambda_1)$. At this point, using a stochastic simulation scheme (such as DPD) is essential. We launch N_1^{shoot} simulations, each using a different random number seed, and each time picking, at random, one of the N_1^{succ} configurations at $\lambda = \lambda_1$ as a starting configuration. Each simulation is continued until it either reaches the next interface or returns to state A. Those that reach the next interface, N_2^{succ} , are saved and used as starting points for the next set of simulations, and $P(\lambda_2 | \lambda_1) = N_2^{\text{succ}} / N_1^{\text{shoot}}$. This procedure is repeated for every interface until reaching B. Figure 4 shows some typical trajectories connecting states A and B and passing through all interfaces λ_i .

FFS also gives insight into the nature of the isocommitator state, i.e., the location where 50% of all trajectories continue to B and 50% return to A. We define $k_{A\lambda} = \Phi_{A,1} \times P(\lambda | \lambda_1)$. As the critical value of the reaction coordinate, λ^* is the one for which the probabilities of ending up in either state A and B are equal, $k_{A\lambda^*} = 2k_{AB}$. In the present case, we study a rare event in a quasiequilibrium system. In that case, FFS can also be used to sketch the free-energy barrier separating states A and B.³¹ We have not done so as this would have required better statistics than could be obtained with the available computing power.

D. Simulation details

We first studied a system containing just water and oil, without surfactants. To study the effect of the water film thickness on the rupture rate, we varied the box length while

keeping the box area, the amount of oil, and the water chemical potential constant. The setup therefore mimics two approaching oil droplets immersed in water (see Fig. 2).

The simulation boxes measured $L_x \times 22 \times 22$, with $L_x = 16, 15.9, 15.8, \dots, 15$. Each system was set up with initially 6300 water beads distributed randomly between $x=5.5$ and $x=L_x-5.5$, and 8032 oil beads on each side. Subsequently, the number of water beads was adjusted by imposing the chemical potential of bulk water at a bead density of 3. The system was then equilibrated in this metastable phase. FFS was then used to drive the system over the free-energy barrier via film rupture. Due to the periodic boundary conditions, the final equilibrium state of this system is a water sphere surrounded by oil. However, this peculiar (artificial) nature of the final state has no effect on the estimate of the coalescence rate.

To study the effect of various surfactants, we started with the metastable oil-water system of $L_x=16$. A total of 776 surfactants were created (388 on each interface) by converting oil beads to tail beads and water beads to head beads, and adding the appropriate intramolecular forces [Eqs. (7) and (8)]. The systems were then reequilibrated in the metastable phase. The total number of hydrophobic beads was thus the same in all the simulations, allowing for a comparison of coalescence rates for droplets at the same separation but with different surface chemistry. Furthermore, the surface density of surfactant was the same ($N_{\text{surf}}/A=0.8$) for the three systems containing surfactant. It was chosen such that the interfaces were fairly saturated with surfactant without surfactants leaving the interface for the bulk.

The conservative forces were integrated using the velocity-Verlet algorithm with $\Delta t=0.03$. The random and dissipative forces were integrated using scheme I of Peters²⁸ with a dissipation amplitude of $\gamma=3.0$.

We used a hybrid DPD-Monte Carlo simulation scheme: At each cycle there is a 2% probability of performing a series of DPD steps and a 98% probability of attempting removal or addition of water beads. In the case of DPD steps, the number of steps is also chosen at random, with a maximum of 100. Thus, on average, the number of DPD steps equals the number of cycles. In the case of particle removal or addition, either is chosen with equal probability and the standard grand-canonical acceptance rules apply.³² The chemical potential was that of bulk water at a bead density of 3: $\mu_w = 13.27$. Particle insertions and removals were performed only during the first part of the FFS scheme, in the equilibrium simulation for collecting configurations at λ_1 . Thus, the number of water particles varied between the sample trajectories, but was fixed along the trajectories from λ_1 to λ_B .

For each system, we first performed a short equilibrium simulation in state A to determine the limits λ_A and λ_1 . We defined λ_A as the average value of λ during this run. λ_1 was chosen such that we would get about 30 crossings of interface 1 within a simulation of 500 000 cycles. During the (longer) equilibrium run, the flux $\Phi_{A,1}$ was computed and the configurations at λ_1 were saved to disk. Depending on the system we used 10–25 interfaces with $N^{\text{shoot}}=100$ –600, and the success rates were typically 0.1–0.5.

The channel radius that can be reached with the current

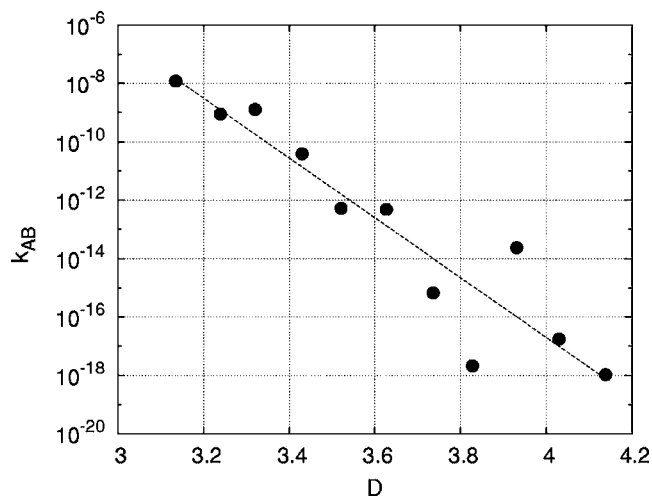


FIG. 5. Film-rupture rates in an oil-water-oil film, without surfactant, as a function of film thickness.

setup is limited by the periodic boundary conditions. However, in all the systems we investigated, $P(\lambda_{i+1}|\lambda_i) \approx 1$ for $\lambda_i > 0.9$. This means that the channel grows spontaneously once its radius reaches $R \approx 0.04L_y$. We can therefore choose state *B* to be a channel with this radius and neglect the effect of the periodic boundary conditions.

Forward flux sampling can also be conducted in a recursive manner, using the branched scheme in Ref. 18. However, we found computing each $P(\lambda_{i+1}|\lambda_i)$ separately more practical, as some trial and error is needed at each interface in order to choose sensible values for N_i^{shoot} and λ_{i+1} .

We also tried other reaction coordinates than the one defined in Appendix A. For systems with relative high film rupture rates, the results were the same (within the statistical errors). For systems with very low rates, alternative definitions of λ were less efficient or failed at driving the system over the free-energy barrier.

IV. RESULTS AND DISCUSSION

A. Film rupture in the absence of surfactant

1. Film rupture rates and the critical state

The film rupture rate depends on the film thickness. We therefore first studied the rupture rate for a water film between two oil phases, without surfactant. The rate as a function of average film thickness D is shown in Fig. 5. D is defined in Appendix B and given in units of r_c . The rate is given in units of film rupture events per unit area per time unit. We use a coarse-graining level where one bead corresponds to about three water molecules. This gives $r_c = 6.46 \text{ \AA}$. The time scale was inferred by equating the simulated and experimental diffusion constant of water: $\tau = 0.088 \text{ ns}$.⁸ Hence, $k_{AB}^{\text{SI}} = k_{AB}^{\text{DPD}} \times 10^{28} \text{ m}^{-2} \text{ s}^{-1}$, giving film rupture rates of $10^{10} - 10^{20} \text{ m}^{-2} \text{ s}^{-1}$.

The scatter in the graph gives an impression of the statistical error. The rate appears to decrease exponentially with film thickness and can be fitted to the expression $k_{AB} = a \exp(-bD)$ with $a = 2 \times 10^{24}$, and $b = 24$.

Figure 6 shows the critical value of λ for each system, λ^* . The figure shows that there is a clear dependence of λ^* on

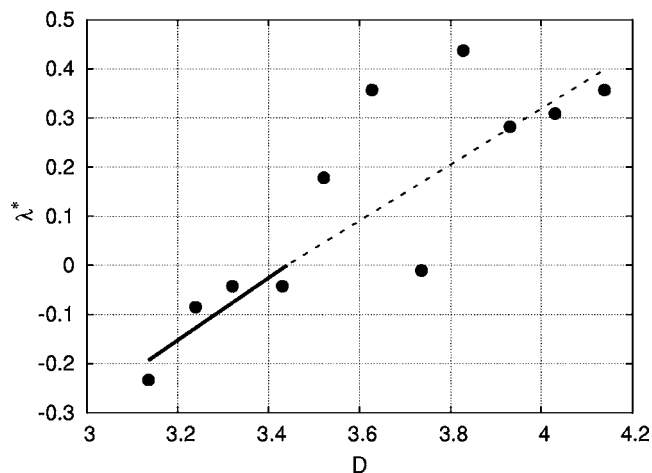


FIG. 6. The critical value of the reaction coordinate vs film thickness D . When λ^* is positive, it denotes a critical channel radius; when it is negative, it denotes the critical local film thickness as defined in Appendix A. The solid line is a fit to the four lowest D -values. The dashed line is a continuation of the solid line with slope as predicted by the channel nucleation theory (see text).

D : Thin water films have a critical (local) film thickness ($\lambda^* < 0$), while thicker water films have a critical channel radius ($\lambda^* > 0$). This means that thick films can heal: If they have a hole of radius λ^* , 50% of the water films break and the other 50% heal and remain intact. In contrast, thin films rupture spontaneously following a sufficiently large thickness fluctuation, and once a hole forms, it always grows.

Note that the local critical water-film thickness, defined by $k_{A\lambda^*} = 2k_{AB}$, differs from what is commonly referred to as the critical film rupture thickness.³³ The former characterizes the smallest fluctuation that leads to rupture of a static film, and it depends on the average film thickness. The latter applies to a dynamic situation where the film is drained. It denotes the average thickness of the film when it breaks and it depends on the draining velocity.

2. Comparison with the channel-nucleation theory

In the absence of surfactant, the bending rigidity of the surface is very low: $(0.0 \pm 0.2)k_B T$.⁷ When $\kappa = 0$, the free energy cost of channel formation is simply the surface tension γ times the difference in surface area between the channel and the two flat surfaces.²⁴

$$F(R, D) = \gamma[2\pi^2 D(R + D) - 4\pi D^2 - 2\pi(R + D)^2]. \quad (14)$$

R and D are the channel radius and the film thickness, respectively. The maximum free energy (the top of the barrier) is then at $R^* = 0.57D$. The dashed line in Fig. 6 has a slope of 0.57, which fits well to the simulation data. However, the intercept is not in agreement with the theory. Note that we cannot expect the same slope for the points with $\lambda^* > 0$ and $\lambda^* < 0$. As it is not entirely clear which points belong to the $\lambda^* > 0$ regime, we have not fitted a line here. However, we fitted the lowest four D -values to get the intercept at $\lambda^* = 0$. This gave $\lambda^* = 0.63(D - 3.4)$ for $\lambda^* < 0$, shown as the solid line in Fig. 6. The dashed line simply shows $\lambda^* = 0.57(D - 3.4)$, or, $\lambda^* + 2.0 = 0.57D$. Thus, according to the theory, the critical radius, R^* , is off by two units (bead radii).

TABLE I. Surface tension, bending rigidity, film-rupture rates, and the critical reaction coordinate for an oil-water-oil film at $L_x=16$. The surface tension values are normalized by the bare oil/water surface tension, γ_0 . k_{AB} is given in DPD units. The surfactants are shown in Fig. 3.

	C ⁻	C ⁰	C ⁺	No surfactant
γ/γ_0	0.39	0.55	0.39	1
$\kappa/k_B T$	1.1	1.2	1.1	0.0
k_{AB}	10^{-8}	10^{-13}	10^{-11}	10^{-18}
λ^*	-0.4	0.2	0.3	0.4

This is large compared to the size of the channel, but some of the discrepancy can be ascribed to the somewhat arbitrary definition of λ in Appendix A. There, the channel radius is defined by the area not covered by the projection of water beads onto the y - z plane. Better definitions of the radius are the radii associated with the equimolar surface R_{em} and the surface of tension R_{st} . In Appendix C we describe simulations to relate the radius defined in Appendix A, R_λ , to R_{em} and R_{st} . These show that $R_{st} \approx R_{em} \approx R_\lambda + 0.7$. We conclude that almost half of the discrepancy between the computed value of R^* and that predicted by the hole nucleation theory can be accounted for by using the surface of tension or the equimolar surface. Nevertheless, it seems that such a small channel is not well described by a macroscopic theory. Another point is that κ might not be exactly zero.

B. The effect of surfactant structure on film rupture

1. Film rupture rates

Table I lists interfacial properties, rupture rates, and the critical values of the reaction coordinate for the surfactants depicted in Fig. 3, and in the absence of surfactant. The surface tension γ and the bending rigidity κ were computed in a separate equilibrium simulation, γ from the pressure tensor and κ from the fluctuation spectrum. Details on these calculations can be found in Refs. 6 and 7.

The rupture rates and the critical reaction coordinates are for oil-water-oil films and $L_x=16$. We find that C⁺ stabilizes the water film better than C⁻ by several orders of magnitude. Note also that C⁻ and C⁺ have the same interfacial properties due to the symmetry of the model. Here, the difference in rupture rates is therefore only an effect of c_0 and is in qualitative agreement with the channel-nucleation theory.

However, we find that C⁰ gives an even lower rupture rate, and the film without surfactant is the most stable of them all. The rupture rate is clearly not only determined by c_0 but also by the interfacial properties. A higher surface tension and/or bending rigidity means less interfacial fluctuations. It seems that such fluctuations are necessary for a channel to form in the first place. Fewer such fluctuations may account for the low coalescence rates for these two systems. We will now present some evidence for this.

FFS gives us not only the final rupture rate, but also some insight into the kinetics of the film rupture process. Figure 7 shows $k_{A\lambda}$, i.e., the rate at which a state with reaction-coordinate λ is reached from A, as a function of λ for each of the four systems. These curves decrease monotonically to the point where the reaction goes

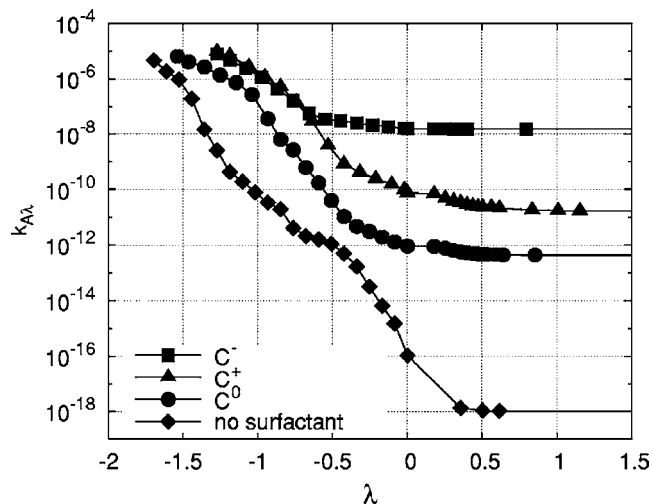


FIG. 7. The rate of reaching the stage described by λ in the film rupture process. The final rupture rate is where $k_{A\lambda}$ levels out.

spontaneously—from there on they are constant. This constant is the final rate listed in Table I. While the final rate is independent of the definition of λ , the $k_{A\lambda}$ curves are not. Nevertheless, they can give us some insight into the free-energy landscape of the reaction, in particular, the location of the top of the barrier and the nature of this state.

First we consider the low λ regime, i.e., where the curves for C⁻ and C⁺ coincide. Here λ is a measure of the minimum film thickness. A channel is not yet formed, and the sign of c_0 does not affect $k_{A\lambda}$ (the magnitude of c_0 does play a role via γ and κ). Because the system is symmetric in oil \rightarrow water and C⁻ \rightarrow C⁺, the curves for these two surfactants coincide as long as the two monolayers do not interact. In the same regime, the difference between the linear (C⁰) and branched (C⁻ and C⁺) surfactants is due to the difference in interfacial properties, rather than natural curvature. The linear surfactant has a higher surface tension and a higher bending rigidity than the branched surfactants. Both these properties suppress the interfacial fluctuations that can lead to channel nucleation. Note that, in the absence of surfactant, the bending rigidity is lower but the surface tension is higher. This results in an even lower rate of fluctuations, i.e., a lower $k_{A\lambda}$.

At $\lambda \approx -0.7$ the curves for C⁻ and C⁺ start to deviate. This is where the two monolayers start to interact. From here until $\lambda \approx 0$, a channel is created, and positive λ values denote the channel radius. The curves for C⁺ and C⁰ are practically parallel in this region. This means that their free energy landscapes are similar. The curve for C⁻ is less steep, implying a lower channel free-energy barrier.

According to Table I, the film without surfactant is the most stable one. This can be explained by the high surface tension that suppresses the fluctuations that lead to film rupture. However, it contradicts the simple observation that surfactant-free dispersions separate very quickly. We discuss this point further in Sec IV B 3.

The results in Table I indicate that an increase in surface tension, bending rigidity, or natural curvature has a negative effect on the coalescence rate. Writing

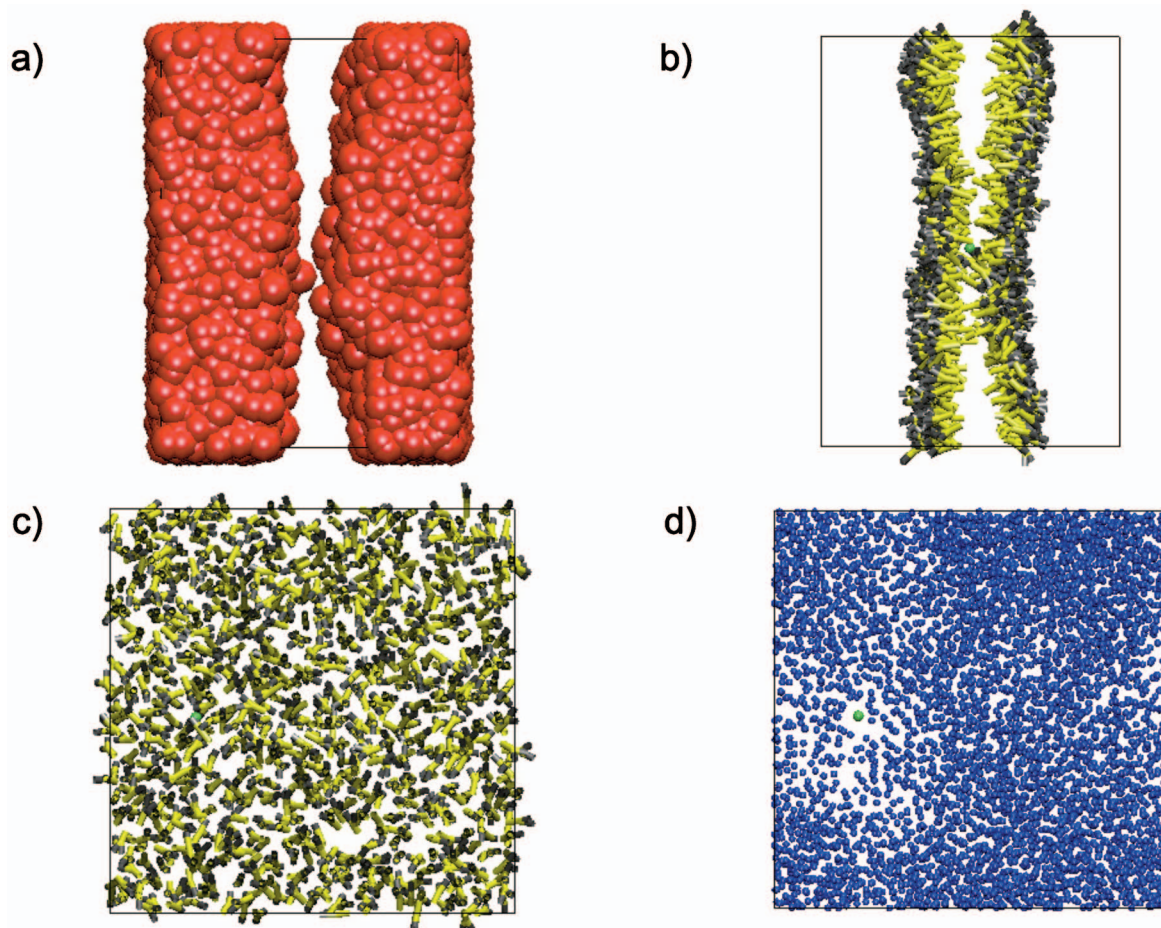


FIG. 8. (Color) Snapshots of the critical configuration for C^- . The green dots in (b), (c), and (d) denote the thinnest point in the film. (a) Oil, xy plane. (b) Surfactant, xy plane. Only bonds are drawn. (c) Surfactant, yz plane. Only bonds are drawn. (d) Water, yz plane. The beads are drawn with a radius of $0.2r_0$ to show the film thinning. (According to the definition of λ there is no hole.)

$$k_{AB} \propto \exp(-\Delta F/k_B T), \quad (15)$$

where ΔF is the free-energy barrier associated with coalescence, we make a simple assumption that the free-energy barrier for coalescence depends linearly on γ and on κc_0 as follows:

$$\log k_{AB} = \alpha_1 + \alpha_2(\gamma/\gamma_0) + \alpha_3 \kappa c_0. \quad (16)$$

We do not know the magnitude of c_0 , but it is nonzero only for C^+ and C^- , for which the product κc_0 differs only in sign. We can therefore rewrite the last term as $\alpha_4 \text{sgn}(c_0)$, where $\alpha_4 \equiv \alpha_3 \kappa$. Based on our four data sets we get $\alpha_1 = -4.5$, $\alpha_2 = -14$, and $\alpha_4 = -1.5$, and the reduced $\chi^2 = 1.2$. More simulations would be needed to verify if this simple approximation has any predictive value.

2. The nature of the critical states

The critical value of the reaction coordinate, defined by $k_{A\lambda^*} = 2k_{AB}$, tells us the location of the barrier maximum. We find that $\lambda^* \approx 0.3$, 0.2 , and -0.4 for C^+ , C^0 , and C^- , respectively. This means that there is a critical channel radius for the film with surfactants of positive and zero natural curvature. The critical stage during film rupture with C^- , however, is much earlier—before the channel forms. In other words,

once a channel forms, it expands spontaneously, without a barrier. These results agree with the channel-nucleation theory.²⁴

Figure 8 shows snapshots of a configuration taken at $\lambda = \lambda^*$ for C^- . For the sake of clarity, each species is shown separately. The first two pictures are viewed parallel to the interfaces, and the last two are viewed perpendicular to the interfaces. The green dots in the three last pictures show the thinnest point in the film. There is no hole in the film, according to the definition in Appendix A, but the film thinning can be seen in the last picture since we have drawn the beads with a smaller radius.

Similarly, Fig. 9 shows snapshots of a configuration taken at $\lambda = \lambda^*$ for C^+ . Here a channel is formed: The two oil phases are in contact (a), and the water film has a hole (c). Now the green area denotes the area of the hole according to the definition in Appendix A. In (e), the water beads are drawn with a reduced radius to show the film thinning around the hole.

Figure 10 shows the region around the critical channel in the system with C^0 surfactant. In (a) one can see that fewer than ten surfactant molecules make up the “stalk” between the two monolayers. In (b) one can locate the channel not as a hole but as a cluster of hydrophobic tails oriented towards each other (indicated by the red circle).

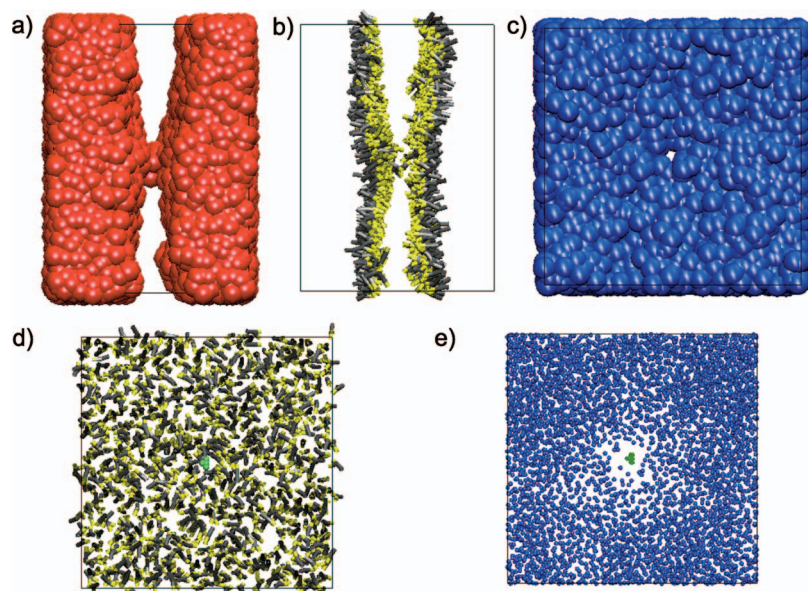


FIG. 9. (Color) Snapshots of the critical configuration for C^+ . The green area in (d) and (f) is the area of the hole, according to the definition of λ . (a) Oil, xy plane. (b) Surfactant, xy plane. Only bonds are drawn. (c) Water, yz plane. (d) Surfactant, yz plane. Only bonds are drawn. (e) Water, yz plane. The beads are drawn with a radius of $0.2r_0$ to show the film thinning around the hole.

3. Discussion

The rates in Table I are given in DPD units and must be multiplied by 10^{28} to convert to SI units ($\text{m}^{-2} \text{s}^{-1}$). They will depend strongly on film thickness, as is evident from Fig. 5. Experimentally, coalescence rates can be determined from the time evolution of the droplet size distributions.^{20,21} However, one can also observe with the naked eye that emulsion lifetimes can vary by many orders of magnitude depending on the surfactant. Kabalnov and Weers²⁵ increased the emulsion lifetime by three orders of magnitude by varying c_0 in the vicinity of $c_0=0$. The c_0 of a nonionic surfactant was varied by adjusting the temperature a mere 0.15°C . With an ionic surfactant, the same was obtained by adding salt. Quantifying c_0 is difficult, both for the model surfactants in this

study and for the real ones. In view of this, we can only state that the rate variations with curvature in Table I appear plausible.

The simulations show that the surfactants affect the film rupture rate in two ways: Due to their lower bending rigidity, asymmetric surfactants increase the interfacial fluctuations necessary to nucleate a channel, compared to a symmetric one. Once a channel is formed, it may or may not expand spontaneously, depending on the sign of the natural curvature caused by the surfactant. This behavior is in agreement with the channel-nucleation theory. The two effects combined result in the following ranking as stabilizers of a water film: C^0 , C^+ , and C^- . The channel-nucleation theory, in contrast, only takes the free energy of the channel state into account. In agreement with this, we find that the critical reaction coordinate λ^* increases monotonically with c_0 .

Our simulations suggest that surfactant-free oil-in-water emulsions would be (meta)stable if nucleation of a critical oil channel in water were the rate-limiting step in coalescence. This finding seems to be at odds with the common observation that a surfactant or another stabilizing agent is needed to prepare a stable emulsion. Apparently, our model system does not capture the relevant mechanism for emulsion breaking in the case of surfactant-free dispersions. We note that there is an important difference between the present DPD model and a real oil-water mixture: the present DPD model cannot undergo capillary evaporation.^{35,36} The reason is twofold: first and foremost, as the number of particles in our DPD simulation is fixed, the “water” phase cannot evaporate, even if the thermodynamic driving force existed. In addition, in real alkane-water systems, dispersion forces play an important role in capillary evaporation: however, such long-ranged forces are absent in the DPD model. We speculate that the coalescence of pure oil droplets in water is a two-step process: first, the liquid water film between two hydrophobic surfaces evaporates due to capillary evaporation. As the oil/air interfacial tension for common alkanes is about 20 mN/m ,³⁴ compared to about 50 mN/m (Ref. 37) for the alkane/water interface, capillary evaporation would substan-

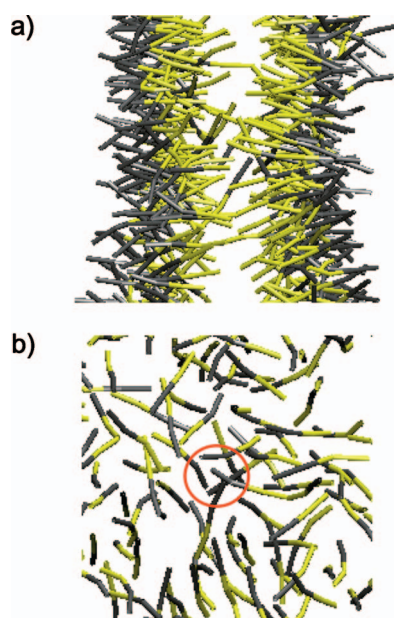


FIG. 10. (Color) A zoom-in on snapshots of the critical configuration for C^0 . Only the bonds are drawn. (a) xy plane. (b) yz plane. The red circle in (b) encircles the cluster of hydrophobic tails that are oriented towards each other and make up the channel.

tially reduce the free-energy cost of subsequent channel formation and consequently increase k_{AB} by many orders of magnitude. In fact, the spontaneous formation of cavities between hydrophobic surfaces has been observed experimentally.³⁸ It is also known that preexisting nanobubbles can coalesce to form vapor bridges between hydrophobic surfaces and this phenomenon has been suggested as the origin of the long-range hydrophobic force.³⁹ Evidence that vapor bridges play a key role in the coalescence of surfactant-free emulsions comes from the observation that the lifetime of a surfactant-free emulsion was greatly enhanced by the removal of dissolved gases, prior to the mixing oil and water.⁴⁰ In our simulations, vapor bridges cannot form because capillary evaporation cannot take place in the (purely repulsive) DPD model of an oil-water mixture. Moreover, even if our model would allow for capillary evaporation or the presence of nanobubbles, the boundary conditions of the present simulations are such that water cannot escape from the film between the oil surfaces. In short, we suggest that the absence of vapor cavities in our simulations explains why we observe such an unexpectedly low film-rupture rate in the absence of surfactant. In the case of surfactant-coated oil droplet, we expect neither capillary evaporation nor the adsorption of nanobubbles on the surface.

V. CONCLUSIONS

We have used dissipative particle dynamics simulations and forward flux sampling to compute film-rupture rates for metastable emulsion films with and without surfactant. For surfactant-free films the rate decreases exponentially with film thickness. Thin films have a critical film thickness and thicker films have a critical channel radius. We also investigated the effect of the natural curvature of the surfactant monolayer on the film-rupture rate. The sign of the curvature determines whether there is a critical channel radius, beyond which the channel grows spontaneously and the film ruptures. The absolute value of the curvature affects the interfacial fluctuations that initiate channel formation. Together they combine to give rupture rates that are nonmonotonic in curvature. Furthermore, we suggest that the absence of vapor cavities in our model system may explain the unexpectedly low film-rupture rates in the absence of a surfactant. Finally, the present study shows that coarse-grained methods such as DPD, augmented with modern approaches to study rare events such as FFS, can give valuable mechanistic insights. It would be interesting to take a similar approach to other related problems, such as hole formation in membranes in electroporation, or the insertion of *trans*-membrane proteins, or the permeation of molecules across lipid membranes.

ACKNOWLEDGMENTS

We thank Dr. Sanne Abeln for useful comments on the manuscript. One of us (L.R.) gratefully acknowledges a grant from The Research Council of Norway. This work is part of the research program of the Stichting voor Fundamenteel Onderzoek der Materie (FOM), which is financially supported by the Nederlandse Organisatie voor Wetenschap-

pelijk Onderzoek (NWO). Computer time at the Dutch center for high-performance computing SARA is gratefully acknowledged.

APPENDIX A: DEFINITION OF λ

The reaction coordinate λ is defined as follows: Before film rupture, it is the negative value of the minimum film thickness. After rupture it is the radius of the area of zero film thickness. We define the local film thickness on a grid with 66×66 nodes and grid size $\Delta = L_y/66$. The thickness at node k is $\tau_k = \frac{2}{3\pi} \sum_i w_{ik}$, where the sum is over all hydrophilic (water and head) beads, $w_{ik} = \max(0, 1 - r_{ik}^2)$ and $r_{ik}^2 = (y_i - y_k)^2 + (z_i - z_k)^2$. The prefactor is chosen such that the average value of τ equals the film thickness D , defined below. If $\min_k \tau_k > 0$, then $\lambda = -\min_k \tau_k$, otherwise λ is defined by $\pi\lambda^2 = N_0\Delta^2$, where N_0 is the number of nodes where $\tau = 0$.

APPENDIX B: DEFINITION OF D

We define the film thickness $D = d_2 - d_1$, where d_1 and d_2 are the Gibbs equimolar interfaces of the water phase including head beads as follows:

$$\int_0^{d_1} (\rho_{w+h}(x) - \rho_{w+h}^{\text{oil}}) dx + \int_{d_2}^{L_x} (\rho_{w+h}(x) - \rho_{w+h}^{\text{oil}}) dx \\ = \int_{d_1}^{d_2} (\rho_{w+h}^{\text{water}} - \rho_{w+h}(x)) dx.$$

Here $\rho_{w+h}(x)$ denotes the average density profile of water and head beads, ρ_{w+h}^{oil} denotes the average density of water and head beads in the bulk oil phase, and $\rho_{w+h}^{\text{water}}$ denotes the average density of water and head beads in the middle of the water film. From density profiles we find that $\rho_{w+h}^{\text{oil}} = 0$ (the hydrophilic beads are practically insoluble in oil) and $\rho_{w+h}^{\text{water}} = 3$ (the density of the bulk reservoir). This means that $D = \langle N_{w+h} \rangle / 3L_yL_z$.

APPENDIX C: THE RELATION BETWEEN R_λ , R_{em} , AND R_{st}

First we determined the relationship between the channel radius as defined by λ in Appendix A, R_λ , and the radius of the equimolar surface. For this we used configurations from the FFS runs where R_λ is known. We defined an instantaneous equimolar surface of the channel by constructing a three-dimensional grid and defining a density

$$\rho(x, y, z) = \sum_i \max(1 - (r/r_c)^2, 0) t_i, \quad (\text{C1})$$

where the sum is over all particles i , r is the particle's distance from the grid point, and t_i is 1 if the particle is a water particle and -1 if it is an oil particle. Points at which $\rho = 0$ defines the surface, but with a finite number of grid points we must choose points with $|\rho| < \rho_{\text{max}}$. The choice of ρ_{max} will depend on the grid resolution, choosing it too low gives few points at the surface, choosing it too high gives a thick surface. At fixed x -values in the vicinity of $x = 0.5L_x$ the points describe circles. We define the "equimolar channel radius" $R_{\text{em}} = \sqrt{A_{\text{em}}/\pi}$, where A_{em} is the area of the smallest

circle (the narrowest part of the channel). We find that $R_{\text{em}} \approx R_{\lambda} + 0.7$.

The surface of tension cannot be calculated during a FFS simulation, but we conducted a separate equilibrium simulation of a small water droplet in oil. The radius of the surface of tension, R_{st} , follows from

$$\Delta P = 2\gamma/R_{\text{st}}, \quad (\text{C2})$$

where ΔP is the pressure difference inside and outside the droplet, and γ is the surface tension of the corresponding flat interface. For a droplet of 150 particles, R_{em}^w and R_{em}^o are both 2.2 ± 0.1 while $R_{\text{st}} = 2.1 \pm 0.3$. This shows that the surface of tension is close to the equimolar surface.

¹J. Sjöblom, *Emulsions and Emulsion Stability* (Dekker, New York, 1996).

²M. J. Rosen, *Surfactants and Interfacial Phenomena*, 2nd ed. (Wiley, New York, 1989).

³R. D. Groot and P. B. Warren, *J. Chem. Phys.* **107**, 4423 (1997).

⁴R. D. Groot and T. J. Madden, *J. Chem. Phys.* **108**, 8713 (1998).

⁵C. J. Wijmans, B. Smit, and R. D. Groot, *J. Chem. Phys.* **114**, 7644 (2001).

⁶L. Rekvig, M. Kranenburg, J. Vreede, B. Hafskjold, and B. Smit, *Langmuir* **19**, 8195 (2003).

⁷L. Rekvig, B. Hafskjold, and B. Smit, *J. Chem. Phys.* **120**, 4897 (2004).

⁸R. D. Groot and K. Rabone, *Biophys. J.* **81**, 725 (2001).

⁹J. C. Shillcock and R. Lipowsky, *J. Phys. Chem.* **117**, 5048 (2002).

¹⁰M. Kranenburg, M. Venturoli, and B. Smit, *J. Phys. Chem. B* **107**, 11491 (2003).

¹¹R. Pool and P. G. Bolhuis, *Phys. Chem. Chem. Phys.* **8**, 941 (2006).

¹²M. Laradji and P. B. Sunil Kumar, *Phys. Rev. Lett.* **93**, 198105 (2004).

¹³J. Koplik and J. R. Banavar, *Science* **257**, 1664 (1992).

¹⁴S. Murad and C. K. Law, *Mol. Phys.* **96**, 81 (1999).

¹⁵M. J. Stevens, J. H. Hoh, and T. B. Woolf, *Phys. Rev. Lett.* **91**, 188102 (2003).

¹⁶L. Rekvig, B. Hafskjold, and B. Smit, *Langmuir* **20**, 11583 (2004).

¹⁷R. J. Allen, P. B. Warren, and P. R. ten Wolde, *Phys. Rev. Lett.* **94**, 018104 (2005).

¹⁸R. J. Allen, D. Frenkel, and P. R. ten Wolde, *J. Chem. Phys.* **124**, 024102 (2006).

¹⁹R. J. Allen, D. Frenkel, and P. R. ten Wolde, *J. Chem. Phys.* **124**, 194111 (2006).

²⁰B. Deminiere, A. Colin, F. Leal-Calderon, J. F. Muzy, and J. Bibette, *Phys. Rev. E* **82**, 229 (1999).

²¹V. Schmitt and F. Leal-Calderon, *Europhys. Lett.* **67**, 662 (2004).

²²W. Helfrich, *Z. Naturforsch. C* **28**, 693 (1973).

²³J. N. Israelachvili, *Colloids and Surfaces A-Physicochemical and Engineering Aspects* **91**, 1 (1994).

²⁴A. Kabalnov and H. Wennerström, *Langmuir* **12**, 276 (1996).

²⁵A. Kabalnov and J. Weers, *Langmuir* **12**, 1931 (1996).

²⁶P. J. Hoogerbrugge and J. M. V. A. Koelman, *Europhys. Lett.* **19**, 155 (1992).

²⁷P. Español and P. B. Warren, *Europhys. Lett.* **30**, 191 (1995).

²⁸E. A. J. F. Peters, *Europhys. Lett.* **66**, 311 (2004).

²⁹C. Lowe, *Europhys. Lett.* **47**, 145 (1999).

³⁰R. D. Groot, *Langmuir* **16**, 7493 (2000).

³¹C. Valeriani, R. J. Allen, M. J. Morelli, D. Frenkel, and P. R. ten Wolde, *J. Chem. Phys.* **127**, 114109 (2007).

³²D. Frenkel and B. Smit, *Understanding Molecular Simulations: From Algorithms to Applications*, 2nd ed. (Academic, San Diego, CA, 2002).

³³I. B. Ivanov, B. Radoev, E. Manev, and A. Scheludko, *Trans. Faraday Soc.* **66**, 1262 (1970).

³⁴J. J. Jasper, *J. Phys. Chem. Ref. Data* **1**, 841 (1972).

³⁵K. Lum and A. Luzar, *Phys. Rev. E* **56**, 6283 (1997).

³⁶K. Lum, D. Chandler, and J. D. Weeks, *J. Phys. Chem. B* **103**, 4570 (1999).

³⁷S. Zeppieri, J. Rodriguez, and A. L. L. de Ramos, *J. Chem. Eng. Data* **46**, 1086 (2001).

³⁸S. Singh, J. Houston, F. van Swol, and C. J. Brinker, *Nature (London)* **442**, 526 (2006).

³⁹E. E. Meyer, K. J. Rosenberg, and J. Israelachvili, *Proc. Natl. Acad. Sci. U.S.A.* **24**, 15739 (2006).

⁴⁰R. M. Pashley, *J. Phys. Chem. B* **107**, 1714 (2003).